Optics Letters

High spatial resolution distributed optical fiber dynamic strain sensor with enhanced frequency and strain resolution

Ali Masoudi* and Trevor P. Newson

Optoelectronics Research Centre (ORC), University of Southampton, Southampton SO17 1BJ, UK
**Corresponding author: a.masoudi@soton.ac.uk*

Received 19 October 2016; revised 21 November 2016; accepted 24 November 2016; posted 28 November 2016 (Doc. ID 278834); published 11 January 2017

A distributed optical fiber dynamic strain sensor with high spatial and frequency resolution is demonstrated. The sensor, which uses the φ-OTDR interrogation technique, exhibited a higher sensitivity thanks to an improved optical arrangement and a new signal processing procedure. The proposed sensing system is capable of fully quantifying multiple dynamic perturbations along a 5 km long sensing fiber with a frequency and spatial resolution of 5 Hz and 50 cm, respectively. The strain resolution of the sensor was measured to be 40 nϵ.

OCIS codes: (060.2370) Fiber optics sensors; (290.5870) Scattering, Rayleigh.

https://doi.org/10.1364/OL.42.000290

The concept of using an optical fiber to map dynamic perturbations along the sensing fiber was first proposed by Taylor and Lee [1] and later demonstrated by their team in 2005 [2]. The proposed sensor was only capable of detecting the dynamic perturbations along the sensing fiber by monitoring the changes in the pattern of the backscattered coherent Rayleigh noise. The volume of research since then has proliferated and has focused on developing distributed optical fiber dynamic strain sensors that are capable of fully quantifying the characteristics of perturbations, such as frequency and amplitude along the sensing fiber. The first distributed optical fiber sensor capable of full characterization of dynamic strains was demonstrated by Song and Hotate [3]. The proposed sensor used Brillouin optical correlation domain analysis (BOCDA) to interrogate 20 m long sensing fiber. Despite its high spatial resolution, the bandwidth of the sensor was limited to 200 Hz mainly due to the slow sensing procedure intrinsic to the BOCDA sensing technique. In addition, the relatively low strain sensitivity of the sensor made it unsuitable for mapping acoustic fields.

Initially, distributed optical fiber dynamic strain sensors had limited dynamic and/or frequency range mainly due to their slow interrogation techniques. In 2013, Masoudi *et al.* demonstrated a long-range and high-bandwidth distributed dynamic strain sensor capable of measuring dynamic vibrations [4]. The proposed sensing technique was based on phase optical time-domain reflectometry (φ-OTDR), a technique which determines the induced strain using the phase of the Rayleigh backscattered light. A detailed review of the past and present measurement techniques capable of fully quantifying the dynamic perturbations and a comparison between their key parameters can be found in [5].

One of the drawbacks of the current sensing systems for mapping acoustic fields has been their relatively high noise floor [4,6]. The main source of noise in these systems is the amplified spontaneous emission (ASE) noise from the two erbium-doped fiber amplifiers (EDFAs) used to amplify the probe pulse and the backscattered light. The ASE noise include ASE-ASE beat noise, signal-ASE beat noise, and ASE-shot beat noise [7] where the noise level in each case depends on the bandwidth of the ASE spectrum. In the previous publications [4,6] two matched fiber Bragg grating (FBG) filters were used to reduce the ASE. The first was placed after the power amplifier used to amplify the probe pulse. The second was placed after the pre-amplifier to amplify the weak backscattered Rayleigh signal. By reducing the linewidth of these two FBGs the ASE noise can be reduced. The practical limit is, however, governed by the stability of the reflection wavelength of the FBGs. For the two FBGs to remain matched the linewidth of both should be larger than the anticipated wavelength drift arising from changes in the temperature of their environment.

In this Letter, a novel optical arrangement is introduced which uses a single narrow FBG to perform both functions, i.e., to reduce the ASE noise from both the power amplifier and pre-amplifier. Unlike the sensing systems with two FBGs, the bandwidth of the FBG used in the new arrangement can be very narrow thereby enhancing the rejection of ASE-generated noise. This new experimental arrangement is combined with an improved signal processing procedure that is less susceptible to noise. Much enhanced results, including a fourfold improvement in spatial resolution, a twofold improvement in strain resolution,

and an eighteenfold improvement in frequency discrimination, are demonstrated.

This Letter begins with a brief description of the underlying sensing principles of the sensor followed by a detailed description of the new signal processing procedure and the experimental setup. Next, the experimental results are presented followed by an analysis of the results and conclusion.

The strain distribution along the sensing fiber is mapped by examining the changes in the phase of the backscattered Rayleigh light [4]. For any given section of the fiber, the phase difference between the backscattered light from the two ends of that section, $\Delta\phi$, is a function of the length of that section, ℓ. For any unperturbed section of the sensing fiber, the length and, consequently, the phase difference remain unchanged. Any perturbation that induces a strain ϵ on the fiber will change the phase difference. The changes in the phase difference as a function of length is given by [8]

$$\Delta\phi(\ell) = \varepsilon\ell\left[\beta - \frac{1}{2}\beta n^2[(1-\mu)p_{12} - \mu p_{11}]\right], \tag{1}$$

where β is the propagation constant of light in the fiber, n is the refractive index of the fiber, μ is the Poisson's ratio, and p_{11} and p_{12} are strain-optic coefficients. Replacing the values of refractive index ($n = 1.456$), Poisson's ratio ($\mu = 0.17$), and strain-optic coefficients ($p_{11} = 0.121$, $p_{12} = 0.27$) in Eq. (1) gives

$$\Delta\phi(\ell) = \varepsilon\ell\beta \times 0.78. \tag{2}$$

Equation (2) illustrates that 22% of the phase change is due to the strain-induced refractive index change in the fiber. Therefore, to accurately calculate the strain rate, $\Delta\phi$ should be divided by 0.78. In order to measure the phase difference between the two end points of each section, an imbalanced Mach–Zehnder interferometer (MZI) is used. A symmetrical 3×3 coupler is employed as the interferometer output coupler to avoid the signal fading problem [4]. It can be shown that the intensity of the light at the three output arms of the MZI is given by [4]

$$\begin{aligned} I_1 &= I_0[M + N\cos(\Delta\phi(\ell))], \\ I_2 &= I_0\left[M + N\cos\left(\Delta\phi(\ell) + \frac{2\pi}{3}\right)\right], \\ I_3 &= I_0\left[M + N\cos\left(\Delta\phi(\ell) - \frac{2\pi}{3}\right)\right], \end{aligned} \tag{3}$$

where I_0 is the intensity of the input signal and M and N are constant. Hitherto, a differentiate and cross-multiplying (DXM) demodulator was used to extract the phase information from the outputs of the three detectors [4,6]. The main drawback of the DXM demodulator is the use of a differentiator in the demodulation process, which is inherently sensitive to noise. In order to avoid the differentiator, a new signal processing procedure is devised to retrieve the phase information using an arc-tangent function and for phase variation beyond $\pm\pi/2$, the new procedure used a fringe-counting algorithm. To retrieve the phase information, the DC components of the three terms in Eq. (3) need to be eliminated first. The DC term can be calculated as follows:

$$S = \frac{I_1 + I_2 + I_3}{3} = I_0 M. \tag{4}$$

Subtracting Eq. (4) from the three terms in Eq. (3) gives

$$\begin{aligned} \dot{I}_1 &= I_0 N\cos(\Delta\phi(\ell)), \\ \dot{I}_2 &= I_0 N\cos\left(\Delta\phi(\ell) + \frac{2\pi}{3}\right), \\ \dot{I}_3 &= I_0 N\cos\left(\Delta\phi(\ell) - \frac{2\pi}{3}\right). \end{aligned} \tag{5}$$

Finally, using trigonometric identities, the phase information can be recovered as follows:

$$\Delta\phi = \arctan\left(\frac{\dot{I}_2 - \dot{I}_3}{\dot{I}_1}\right). \tag{6}$$

A fringe-counting algorithm is implemented by looking at the transition of $\Delta\phi$ from $+\pi/2$ to $-\pi/2$ and vice versa.

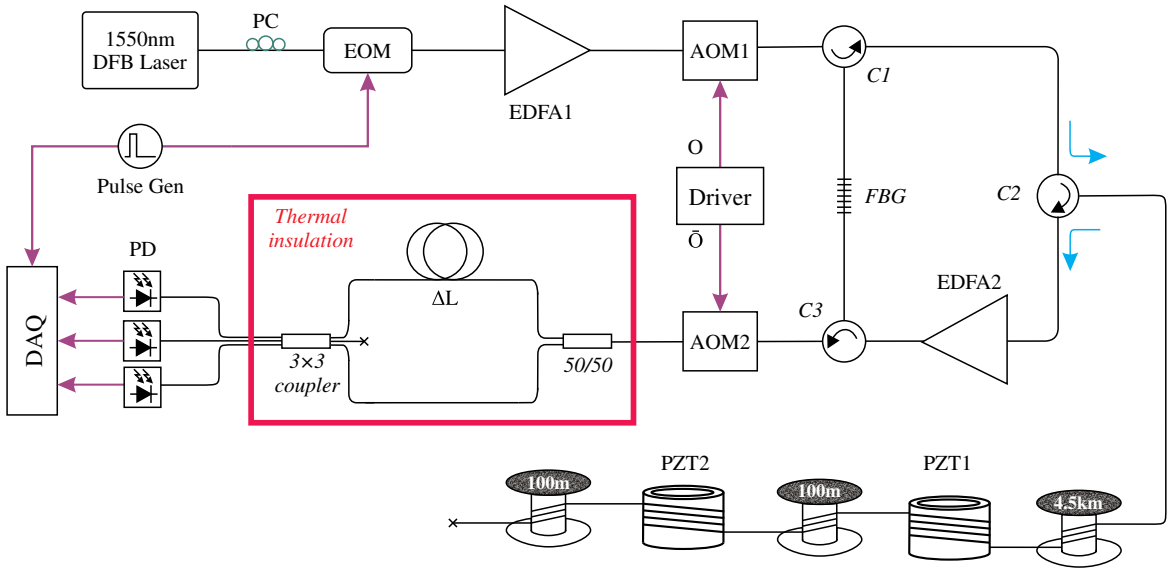

Fig. 1. Experimental setup. DFB, distributed feedback; PC, polarization controller; EOM, electro-optic modulator; EDFA, erbium-doped fiber amplifier; AOM, acousto-optic modulator; C, circulator; FBG, fiber Bragg grating; PD, photodetector; DAQ, data acquisition system.

The experimental setup is shown in Fig. 1. A 1550 nm distributed feedback laser diode was modulated with an electro-optic modulator to generate a 5 ns pulse with a repetition rate of 50 μs. The pulse was then amplified by an erbium-doped fiber amplifier (EDFA1) to raise the peak power to 4 W. The amplified pulse was passed through an acousto-optic modulator (AOM1) (insertion loss = 3 dB; extinction ratio = 50 dB) followed by an FBG filter ($\lambda_B = 1550.52$ nm; $\Delta\lambda = 0.2$ nm; reflectivity = 99.9%) to remove the ASE from the EDFA1 via circulator C1. The probe pulse with peak power of 2 W was then launched into the sensing fiber via circulator C2. The sensing fiber consisted of a 4.9 m and a 2.4 m long single-mode fiber wrapped around two piezoelectric ceramics (PZTs) (PZT1: a 155 mm diameter ring PZT; PZT2: 115 mm diameter ring PZT) separated by a 100 m unstrained–unheated fiber. A 4.5 km and a 100 m long unstrained–unheated fiber were used to separate the PZTs from the front end and far end of the sensing fiber, respectively. The backscattered Rayleigh signal was collected by the circulator C2 and amplified by the second optical amplifier (EDFA2). The ASE from the second optical amplifier was filter by the same FBG used to filter the ASE of the first optical amplifier via circulator C3. For use in environments with temperature variations greater than (10°C), the FBG should be temperature stabilized.

The experimental procedure went through two phases during each interrogation cycle: the pulse-formation phase and the signal-detection phase. The control signals to the two AOMs were adjusted accordingly to direct or block the light during each phase. During the pulse-formation phase, AOM1 was switched on to allow the probe pulse to reach the sensing fiber. During this period, AOM2 remained switched off to block the ASE of EDFA1 from saturating the detectors. If AOM2 does not block the light, the entire ASE spectrum from EDFA1 less 0.2 nm (i.e., FBG bandwidth) passes through the FBG and falls on the detectors. During the signal-detection phase, AOM1 was switched off to isolate the pulse-formation arm of the sensor and AOM2 was turned on to allow the amplified backscattered light through to the MZI after it had been filtered by the FBG to remove ASE generated by EDFA2.

After passing through AOM2, the filtered backscattered signal was fed into the thermally insulated MZI with path imbalance of 1 m using a 50/50 coupler. Three photoreceivers (40 V/mA transimpedance; 125 MHz bandwidth) were used to detect the light from the 3 × 3 coupler at the output of the MZI. The photoreceivers were sampled using a 250 MHz oscilloscope at a sampling rate of 625 MSa/s.

The 3D diagram of Fig. 2 illustrates the frequency components present in a 300 m section of the sensing fiber between 4500 and 4800 m. The plot represents the post-processed data obtained from the setup while the large and small PZTs were modulated with 1500 and 2000 Hz sinusoidal signals, respectively. The amplitude of the voltage applied to the large PZT was 7 V_{PP} and that of the smaller PZT was set to 10 V_{PP}.

The phase shift and strain level of the larger PZT as a function of the PZT voltage is shown in the diagram of Fig. 3. This diagram demonstrates the PZT response to 1 kHz sinusoidal signals with voltages varying from 1 V_{PP} to 8 V_{PP}. The data points on this figure represent the peak of the strain measured by the sensor.

Figure 4 represents the frequency response of the larger PZT measured by both the distributed sensor (red data points) and MZI (solid line). The solid line is obtained by characterizing the large PZT using cw light and a conventional MZI. The data was collected by applying a fixed voltage (7 V_{PP}) to the PZT while changing the frequency from 100 Hz to 3 kHz.

To assess the spatial and frequency resolution of the sensor, the 3D diagram illustrating the output of the sensor is presented by two 2D diagrams in Fig. 5. Figure 5(a) shows the

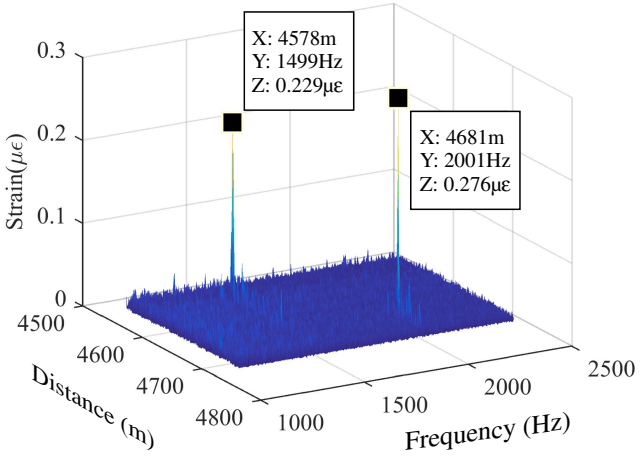

Fig. 2. Frequency components present along a 300 m stretch of the sensing fiber between 4500 and 4800 m.

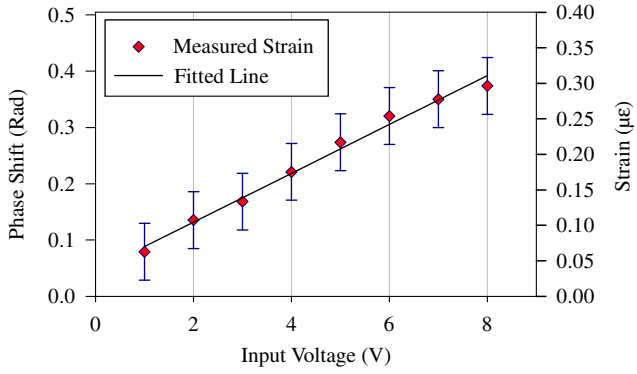

Fig. 3. PZT input voltage versus sensor output for 1 kHz sinusoidal signal.

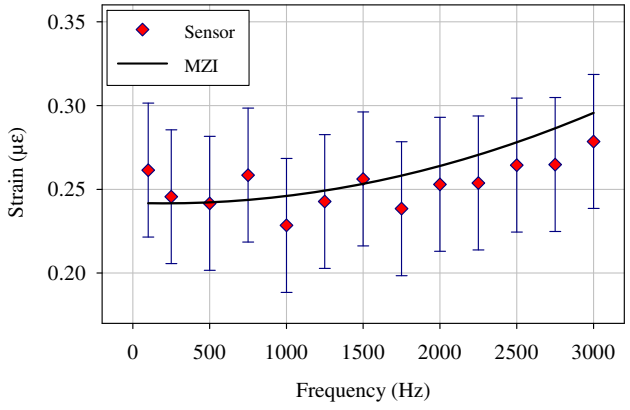

Fig. 4. Frequency response of the large PZT measured by the distributed sensor (red data points) and MZI (solid line).

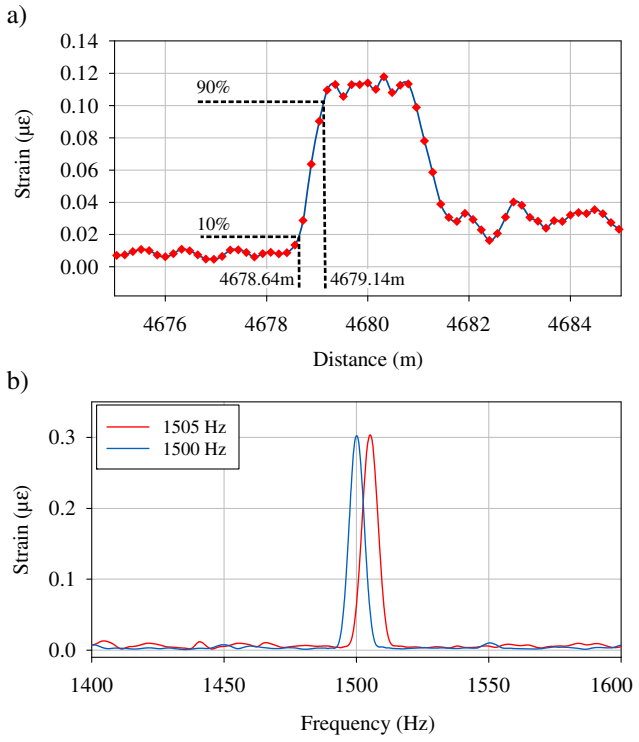

Fig. 5. 2D representation of the 3D diagram depicting the output of the sensor. (a) Spatial distribution of strain along the sensing fiber at 1 kHz. (b) Frequency spectrum of the dynamic fluctuations at 4578 m for 1500 Hz signal (blue trace) and 1505 Hz signal (red trace).

spatial distribution of strain along the sensing fiber at a fixed frequency while Fig. 5(b) shows the frequency spectrum of the dynamic fluctuations at a single point on the sensing fiber. The trace representing the spatial distribution of strain in Fig. 5(a) was obtained by averaging the data acquired from 10 separate measurements. The frequency and amplitude of the input voltage to PZT2 was kept constant at 1 kHz and 8 V_{pp}, respectively, for the duration of the 10 measurements. To measure the frequency resolution, the frequency of the input signal to PZT1 was changed in 1 Hz steps from 1500 to 1505 Hz while monitoring the frequency spectrum of a fixed point on the sensing fiber. Figure 5(b) shows the data acquired for input frequencies of 1500 and 1505 Hz.

The two peaks in Fig. 2 correspond to the strains applied by the two PZTs at 4578 and 4681 m. The 3D plot demonstrates that the sensor can accurately measure the location, frequency, and amplitude of dynamic perturbations along the fiber.

Figure 3 shows a linear relationship between the amplitude of the input voltage to the PZT and the measured phase shift for 1 kHz sinusoidal signal. Equation (2) was used to calculate the strain level shown on the right vertical axis of this diagram:

$$\varepsilon = \frac{\Delta\phi}{0.78\ell\beta} = \frac{\Delta\phi}{0.78\ell}\cdot\frac{\lambda}{2\pi n}, \tag{7}$$

where $\lambda = 1550$ nm, $n = 1.456$, and ℓ is determined by the path imbalanced of the MZI and is equal to $\ell = \Delta L/2 = 0.5$ m. Similar experiments at other frequencies (i.e., 500, 1500, and 2000 Hz) exhibit the same linear characteristic. The minimum detectable strain at 1 kHz was measured to be 40 nε, which shows a factor of 2 improvement from the previous work. Figure 4 shows a good correlation between the data collected with the sensor and the frequency response measured by the MZI. The experimental result also shows that the system can detect frequencies as high as 5 kHz. Based on the observation from Figs. 3 and 4, it can be concluded that the modified sensing arrangement is capable of quantifying the frequency, amplitude, and location of dynamic perturbations anywhere along the sensing fiber with an accuracy of 40 nε. The strain sensitivity of the sensor can be further improved through averaging in expense of a more limited frequency range.

The other advantage of the modified optical arrangement is that it facilitates the development of a wavelength-division multiplexing sensing system that offers improved frequency and/or sensing range. Such a system can be realized by using a multi-wavelength source and only one FBG for each wavelength in the link between circulator C1 and C3.

The analysis of Fig. 5(a) demonstrates 10/90% spatial resolution of 50 cm, a factor of 4 improvement on what was achieved previously. Furthermore, Fig. 5(b) shows that two frequencies as close as 5 Hz can be clearly distinguished from one another. A 5 Hz frequency resolution indicates a factor of 18 improvement from the previous results. The improvement in the frequency resolution was achieved by increasing the acquisition time from 10 to 200 ms.

In summary, the modified experimental setup demonstrated a factor of 4 improvement in gauge length and a factor of 2 improvement in minimum detectable strain. The higher sensitivity was achieved by (1) using a single narrow-bandwidth FBG to filter the ASE from both EDFAs and, (2) eliminating the differentiator from the phase demodulator, which made it inherently less sensitive to noise. The new signal processing procedure was not only less sensitive to noise but also simpler to implement. As a result, the signal processing run time of the new demodulator was 10 times as fast as the DXM demodulation algorithm. The frequency resolution and sensing range of the new setup were measured to be 5 Hz and 5 km, respectively, which indicates a factor of 18 improvement in the frequency resolution and a factor of 5 improvement in the sensing range.

All data supporting this study are openly available from the University of Southampton repository in Dataset 1, Ref. [9].

Funding. Engineering and Physical Sciences Research Council (EPSRC) (EP/N00437X/1).

REFERENCES

1. H. F. Taylor and C. E. Lee, "Apparatus and method for fiber optic intrusion sensing," U.S. patent 5,194,847 (March 16, 1993).
2. J. C. Juarez, E. W. Maier, K. N. Choi, and H. F. Taylor, J. Lightwave Technol. **23**, 2081 (2005).
3. K. Y. Song and K. Hotate, IEEE Photon. Technol. Lett. **19**, 1928 (2007).
4. A. Masoudi, M. Belal, and T. P. Newson, Meas. Sci. Technol. **24**, 085204 (2013).
5. A. Masoudi and T. P. Newson, Rev. Sci. Instrum. **87**, 011501 (2016).
6. C. Wang, C. Wang, Y. Shang, X. Liu, and G. Peng, Opt. Commun. **346**, 172 (2015).
7. K. De Souza and T. P. Newson, Opt. Express **12**, 2656 (2004).
8. G. B. Hocker, Appl. Opt. **18**, 1445 (1979).
9. http://doi.org/10.5258/SOTON/401728.